On the Noise Generation Mechanisms of Side-by-Side Rotors Operating Near Ground

Aeroacoustics Conferences
June 4-7, 2024, Rome, Italy
30th AIAA/CEAS Aeroacoustics Conference (2024)

10.2514/6.2024-3095

On the Noise Generation Mechanisms of Side-by-side Rotors Operating Near Ground

Yan Wu *, Daniele Ragni † and Damiano Casalino ‡
Delft University of Technology, Delft, 2629 HS, The Netherlands

Francesco Avallone §
Politecnico di Torino, Corso Duca degli Abbruzzi, 10129, Torino, Italy

This study presents a numerical investigation of the aerodynamic and aeroacoustics behavior of side-by-side rotors in proximity to the ground. The configuration developed in the European H2020 project ENODISE is used as a reference. It features two counter-rotating APC 6x4 propellers, positioned at a height H/R = 2 above the ground, where R is the propeller radius, with a tip-to-tip distance S/R = 2, operating at a rotational speed of 167 Hz. Scale-resolved simulation is carried out using the Lattice-Boltzmann/Very-Large-Eddy-Simulation CFD solver SIMULIA PowerFLOW®. Analysis of the data describes the spatio-temporal of the flow field and describes in detail the bi-stable behavior of wake in the presence of the ground, which is then re-ingested by the rotor disks. This motion, occurring at a frequency two orders of magnitude lower than the rotor blade passing frequency, is similar to what was found experimentally. In addition, the present work shows the impact of this phenomenon on far-field noise by comparing sound pressure levels (SPL) pre- and post-re-ingestion in a semi-spherical manner. The findings reveal a significant increase in SPL across a broad frequency range as the occurrence of the re-ingestion.

Nomenclature

BPF	=	blade passage frequency
c	=	blade chord
C_p	=	pressure coefficient
GCI	=	grid convergence index
H	=	height above the ground plane
k	=	turbulent kinetic energy
M	=	refinement ratio
N	=	order of convergence
O	=	origin of the spherical system
p	=	static pressure
p_∞	=	free stream static pressure
R	=	rotor tip radius
R	=	radial distance of the spherical system
OSPL	=	overall sound pressure level
S	=	rotor tip-to-tip distance
SPL	=	sound pressure level
t0	=	initial time for record the movement of fountain flow
V_∞	=	free stream velocity
V_{mag}	=	velocity magnitude
W	=	axial velocity

*Postdoc Researcher, Section Wind Energy, Faculty of Aerospace Engineering, Y.Wu-10@tudelft.nl.
†Associate Professor, Section Wind Energy, Faculty of Aerospace Engineering, d.ragni@tudelft.nl, and Member of AIAA.
‡Professor, Section Wind Energy, Faculty of Aerospace Engineering, D.Casalino@tudelft.nl, and Member of AIAA.
§Professor, Department of Mechanical and Aerospace Engineering, francesco.avallone@polito.it, and Member of AIAA.

W_{ind} = induced axial velocity
y^+ = dimensionless wall distance
δx = finest voxel size
θ = polar angle of the spherical system
ϵ = turbulent dissipation rate
λ_2 = lambda-2 vortex criterion
ρ_0 = air density
ϕ = azimuthal angle of the spherical system

Subscripts

b = propeller blade

I. Introduction

The rapidly growing industry of electric-powered Unmanned Aerial Vehicles (UAVs) raises a potential noise issue that could be detrimental to the health of the population. Therefore, prioritizing the understanding of the noise generation mechanisms becomes crucial for developing systems that will be accepted by society. Noise generated by UAVs is influenced by factors such as their size, configurations, operating conditions, and the number of rotors.

The side-by-side rotors configuration is commonly used in multi-rotor UAVs. Tinney and Sirohi [1] conducted experiments in an anechoic chamber, examining isolated rotors as well as quadcopter and hexacopter configurations with propeller diameters ranging from 8" to 12". Their findings showed differences in the blade passage frequency (BPF) harmonic tones between isolated propellers and multi-rotor configurations, which were attributed to acoustic and aerodynamic interference effects between propellers. In another study, Zhou and Fattah [2] conducted acoustic measurements using two 9.4" diameter propellers in an anechoic chamber. They observed a 10 dB noise variation based on the phase difference between the two propellers. Additionally, their results demonstrated minimal impact on the noise level due to changes in rotor tip-to-tip distance. Further investigation was carried out by Schiller *et al*. [3] that studied two 2-bladed rotors controlling the phase angle between the two rotors. Their findings indicated that co-rotating rotors offered more benefits in terms of noise reduction compared to counter-rotating rotors, particularly when there was a 90° phase difference. In a recent experimental study, Bu *et al*. [4] conducted investigations in an anechoic chamber, focusing on a side-by-side rotors configuration. Their results indicated that the impact of interactions between two rotors can be neglected on both mean thrust and the harmonic of BPF tones.

Aeroacoustic investigations on small-scale isolated rotors operating in ground effect (IGE) have been recently conducted experimentally [5]. Results show an increase of the broadband noise compared to the one measured for isolated rotor in hover and out of ground effect (OGE). This was attributed to the acoustic reflections from the ground plane. Moreover, because of the presence of the ground, the propeller wake does not develop downstream and can interact with the rotor, thus inducing unsteady loading and subsequently additional noise at higher harmonics of the BPF. A similar finding was reported by Smith *et al*. [6] who conducted a numerical investigation of dual rotors operating IGE.

When a multi-rotor system operates close to the ground, there is a significant, up to 30%, increase in thrust compared to a single-rotor in a free field. However, this increase depends on the tip-to-tip distance (S) and the height (H) above the ground plane. He and Leang [7] observed a 8% reduction in thrust when the multi-rotor system operated with S = 2R (R is the propeller radius) and H = 2R, compared to an OGE condition. When the rotor hovers in proximity to the ground plane, the wake of the rotor spreads radially and forms a wall jet. However, when two rotors are present, the two wall jets create a stagnation region leading to the formation of a fountain flow. Dekker *et al*. [8, 9] recently studied the change in performance because of the fountain flow. They observed a periodic movement of the fountain from one rotor to the other. This motion was attributed to the increasing wake momentum upon the re-ingestion of the fountain by the rotor, leading to an oscillation of the fountain flow root between the two rotors. The cycle frequency was reported to be up to 2 orders of magnitude lower than the BPF. It was shown that this phenomenon significantly affects the aerodynamic performance of the rotors, due to the considerable turbulent flow re-ingestion and resulting unsteady loading on the blade.

The noise generation mechanism for rotor blades interacting with turbulent inflow has been investigated both experimentally [4, 10, 11] and numerically [12, 13]. Results suggest that turbulent inflow-induced unsteady loading results in a significant increase in the SPL values at the harmonics of the BPF across a broad frequency range. The aim of this paper is to clarify how the noise generated by a side-by-side rotor configuration in ground effect depends on the aerodynamic performance change of the rotors under re-ingestion of the fountain flow. The structure of this paper is: Section II describes the methodology employed in the current study. Section III introduces the numerical simulation

setup, and section IV presents the flow field and the acoustic results. The last section summarizes the main conclusions from the paper.

II. Methodology

A. Flow Solver

The high-fidelity computational fluid dynamic (CFD) simulation is carried out using the Lattice-Boltzmann/Very-Large-Eddy-Simulation (LBM/VLES) solver SIMULIA PowerFLOW ®. The LBM has been proven to be accurate in predicting the aerodynamic and aeroacoustics performance in various applications, such as small-scale UAV propellers [14–16], wind turbines [17], and turbofan [18]. A detailed description of this solver can be found in previous works [19–21].

The LB method characterizes the motion of fluid particles at a mesoscopic scale by statistically tracking the advection and collisions of particles through distribution functions. These distribution functions are oriented along a finite set of predefined discrete directions. In the low-speed version of the solver, 19 discrete velocity directions in 3 dimensions (D3Q19) are possible. A third-order truncation of the Chapman-Enskog expansion is adopted. This has been shown to provide sufficient lattice symmetry to recover the Navier–Stokes (NS) equation for a low Mach number isothermal flow [22].

A Very Large Eddy Simulation (VLES) model is implemented to account for the effect of the sub-grid unresolved scales of turbulence. The basic idea is to introduce the eddy viscosity model into the collision term of the LB equation [23]. Following Ref. [24], a two-equation k - ϵ re-normalization group is employed to compute a turbulent relaxation time added to the viscous relaxation time. In order to reduce the computational cost, a pressure-gradient-extended wall model is used to approximate the no-slip boundary condition on solid walls [23, 25]. The model is based on the extension of the generalized law-of-the-wall model [26] to take into account the effect of the pressure gradient.

B. Acoustic Solver

The prediction of the acoustic far-field is evaluated using Ffowcs Williams & Hawkings' (FW-H) acoustic analogy [27]. The solution to this equation is in the form of Farassat's formulation 1A (F1A) [28], which is solved in the time domain using a forward time algorithm [29]. This involves integrating the unsteady pressure on the solid surfaces of the moving body to predict the noise contributed by the thickness (monopole) and loading (dipole) sources. This method is referred to as the solid FW-H approach. An alternative method, known as the permeable FW-H approach, has been introduced by Di Francescantonio [30]. This method extends the FW-H analogy by incorporating a control flow permeable surface encompassing all sources. As a result, in addition to the acoustic monopole and dipole sources, the non-linear contribution of the quadrupole source term related to unsteady turbulence within the surface is also considered. Both solid and permeable FW-H approaches are carried out using the software SIMULIA PowerACOUSTICS ®.

III. Simulation setup

The present simulation replicates the experimental studies by Dekker *et al.* [8, 9]. The simulation comprises two counter-rotating propellers, each having a radius of R = 76.2 mm, placed within an enclosed simulation domain to maintain consistency with the prior experimental setup. These propellers are located at H = 2R above a ground plane with a tip-to-tip distance of S = 2R and rotate at a constant shaft speed of 167 Hz. The current simulation imposes zero initial phase difference between the two propellers. The propellers used in the simulation are commercially available from the APC6X4E series, along with their identical mirrored counterparts from the APC6X4EP series.

This simulation is conducted in a 2 m × 2 m × 3 m domain. The outer boundaries of the domain have frictionless walls. The ground plane covers an area of 0.5 m^2, and is positioned with its center overlapping the origin of the simulation domain. Moreover, a rectangular-shaped flow-permeable surface with dimensions 7.6R × 3.6R × 2.7R is utilized for the permeable FW-H approach. To minimize the backward reflection of acoustic waves from the outer boundary, two spherical-shaped acoustic sponge regions are used, see Fig. 1. These regions are positioned at radii ranging from 6.1R to 11R and centered 1R above the ground plane. The approach gradually increases the value of fluid kinematic viscosity from its physical value within the inner sphere region and then exponentially up to an artificially set value of two orders of magnitude higher beyond the outer sphere region. For convenience, a spherical coordinate system is introduced here. The origin of this coordinate system is denoted by O, located at the midpoint of the line connecting the rotational centers of two rotors. R, ϕ and θ represent the observer position in the radial, azimuthal, and

polar directions, respectively. Additionally, 7 fluid probes are placed at the near-field on the rotors' mirror plane at a radius R = 3R with polar angles ranging from $\theta = 30°$ to 120° to validate the acoustic results predicted from both solid and permeable FW-H approaches.

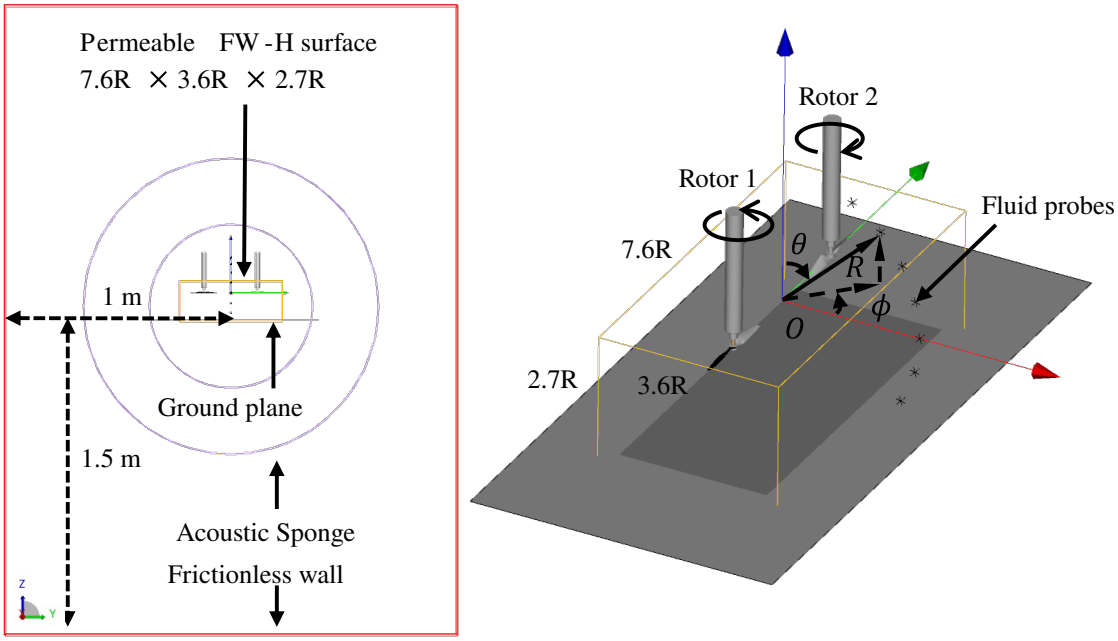

Fig. 1 Schematic of simulation domain.

The simulation domain is discretized into 11 different variable resolution (VR) levels, ranging from the coarsest resolution VR0 to the finest VR10, see Fig. 2. VR10 to VR8 is set close to the blade. Additionally, VR7 is applied to resolve the regions enclosing the rotor's local reference frame (LRFs) and the boundary layer of the ground plane. The voxel resolution between each adjacent VR level varies by factor 2 with a guaranteed minimum of 6 voxels between two adjacent VR regions. Simulations have been carried out by considering four values of global refinement, as reported in Table 1. For the fine grid simulation, the smallest voxel length of δ_x = 0.025 mm is employed, which corresponds to a resolution of 425 voxels along the chord, c, at a blade radius of 0.75R. This results a mean y^+ value of approximately 3.5 for the first voxel height adjacent to the surface of the rotor blade. For this simulation, the physical time step, corresponding to a Courant-Friedrichs-Lewy (CFL) number of 1 in the finest voxel resolution was 4.16×10^{-8} s. The computational cost was about 1.02×10^4 CPU hours/rev on a 575 cores cluster.

To study the motion of the fully developed fountain flow, the very coarse simulation was conducted for 0.53 s of physical time, which is equivalent to 88 rotor revolutions. Furthermore, the results obtained from the instantaneous flow field of the entire fluid domain after the 88$^{\text{th}}$ rotation were utilized to initialize the entire fluid domain for the simulations with finer grid resolution. The relevant flow data were sampled after a settling time of 2 propeller revolutions. Note that the grid refinement was applied uniformly across the simulation domain for each resolution level. The information on voxel size, sampling time and computational cost of these simulations are provided in Table 1 below.

Table 1 Computational information of different resolutions of simulations

Simulation	Resolution ($\frac{c}{\delta_x}$), y^+	Fine equivalent voxels	Sampling time in revolutions	CPU hours/rev
Very coarse	75, $y^+ = 20$	4.5 million	84	287
Coarse	212, $y^+ = 7$	35 million	30	1.87×10^3
Medium	300, $y^+ = 5$	73 million	14	3.77×10^3
Fine	425, $y^+ = 3.5$	160 million	14	1.02×10^4

For acoustic prediction, the solid FW-H approach was applied to the propellers, hubs, and upper surface of the ground plane. The data was sampled at a frequency of 100 kHz with an averaging spatial resolution of 0.5 mm on

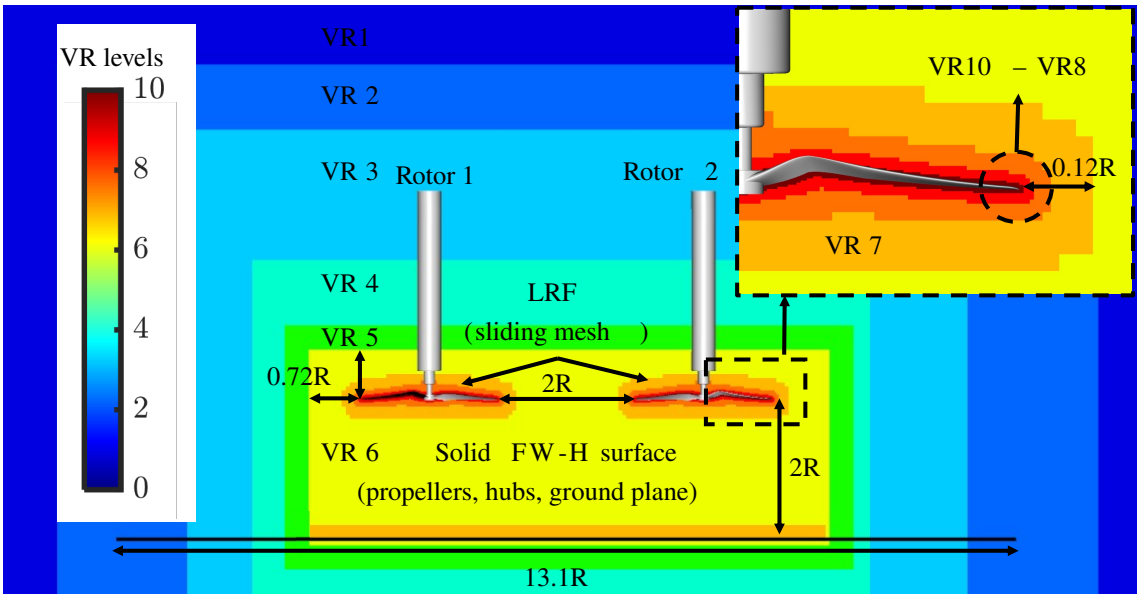

Fig. 2 Sketch of computational setup and VR level distributions.

the solid surface. This level of resolution, even in the very coarse grid simulation, proved to be sufficient in resolving acoustic pressure up to 15 kHz, ensuring at least 6 voxels per wavelength. Additionally, the simulation for an isolated rotor configuration IGE was performed by removing rotor 2 from the present dual rotor configuration while keeping all other setup parameters identical. For ease of reference, the dual rotor configuration IGE and isolated rotor configuration IGE are hereafter referred to as DIGE and IIGE, respectively.

Acoustic far-field measurements were performed using 468 virtual microphones, placed in a semi-spherical configuration at a distance of 20R from the origin O. These microphones were uniformly distributed in the azimuthal direction, spaced every 10 degrees from $\phi = 0^\circ$ to 360°, and in the polar direction spaced every 5 degrees from $\theta = 30^\circ$ to 90°, as illustrated in Fig. 3 below. Where the ground plane and two rotors are depicted by the black rectangular and two circles, respectively. The two red circles indicate the position of the microphones at different azimuthal and polar angles.

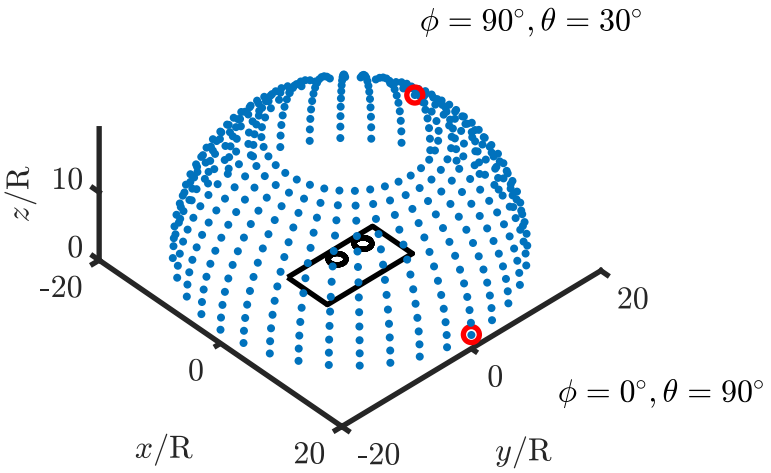

Fig. 3 Acoustic far-field measurement microphones distribution.

IV. Results and Discussion

A. Results Validation

The time-history of thrust, for the very coarse grid simulations, for both IIGE and DIGE cases are illustrated in Fig. 4. In sub-figure (a), the average thrust for the rotor from the IIGE is around 1.8 N after the 4$^{\text{th}}$ rotation. Conversely, the results for the rotors from the DIGE are nearly identical to the results from the IIGE before the 16$^{\text{th}}$ rotation, as no flow re-ingestion occurs. After around the 16$^{\text{th}}$ rotation, the thrust for dual rotors begins to fluctuate, experiencing a slight drop before stabilizing relatively around 1.76 N after the 65$^{\text{th}}$ rotation. This is made clearer in sub-figure (b), where the fluctuation values of the thrust for the rotors from the DIGE gradually increase to approximately 0.05 N after the 60$^{\text{th}}$ rotation, as indicated by the time-history of the standard deviation (SD) of the thrust. Fewer variations are observed for the rotor from the IIGE, with the SD of thrust remaining at a similar level of around 0.025 N. Notably, the SD of thrust for an additional 14 rotations obtained from the simulation with a $y^+ = 3.5$ is 0.047N for DIGE and 0.034 N for IIGE, respectively. These results show a relatively statistically convergence for the current simulation setup, particularly indicating that the fountain flow has fully developed for DIGE. The re-ingestion effect can result in a drop of rotor thrust, which is also observed for the fine grid simulations with a 1.4% offset compared to 2.02 N from the DIGE to 2.05 N from the IIGE.

A grid-independence study is conducted for the DIGE case. Both aerodynamic and aeroacoustics parameters have been verified. Results are shown for the four grid resolutions, with the corresponding y^+ values. Fig. 5 shows the time-averaged mean thrust of two rotors for the four resolutions; data show a converging trend increasing resolution. In the figure, the red square, corresponding to y^+ equal to 0 show the asymptotic value of thrust obtained using the Richardson extrapolation. It is calculated using the results obtained from y^+ values of 7, 5, and 3.5 with a uniform refinement ratio $M = \sqrt{2}$ and the order of convergence $N = 2.5$. This demonstrates a reasonably good agreement with the experimental results of 2.14 N [9], with an error of 4.5%. Furthermore, the convergence is evaluated using the value of grid convergence index (GCI) [31], as defined in eq. 1. For this study $\mathrm{GCI}_{(3.5,5)} = 0.013$, $\mathrm{GCI}_{(5,7)} = 0.032$ with the GCI ratio equals 1.012 is approximately equal to 1, indicating solutions within the asymptotic range of convergence.

$$\mathrm{GCI} = \frac{\mathrm{GCI}_{5,7}}{M^N \mathrm{GCI}_{3.5,5}} \tag{1}$$

Fig. 6 illustrates the comparison of SPL spectra in one-third octave bands obtained with different grid resolutions at an observer distance of 3R from the origin O at polar angle $\theta = 45°$ and azimuthal angle $\phi = 0°$. The SPL values are calculated using the solid FW-H method. The curves of different resolutions are in similar trend, and a clear convergence

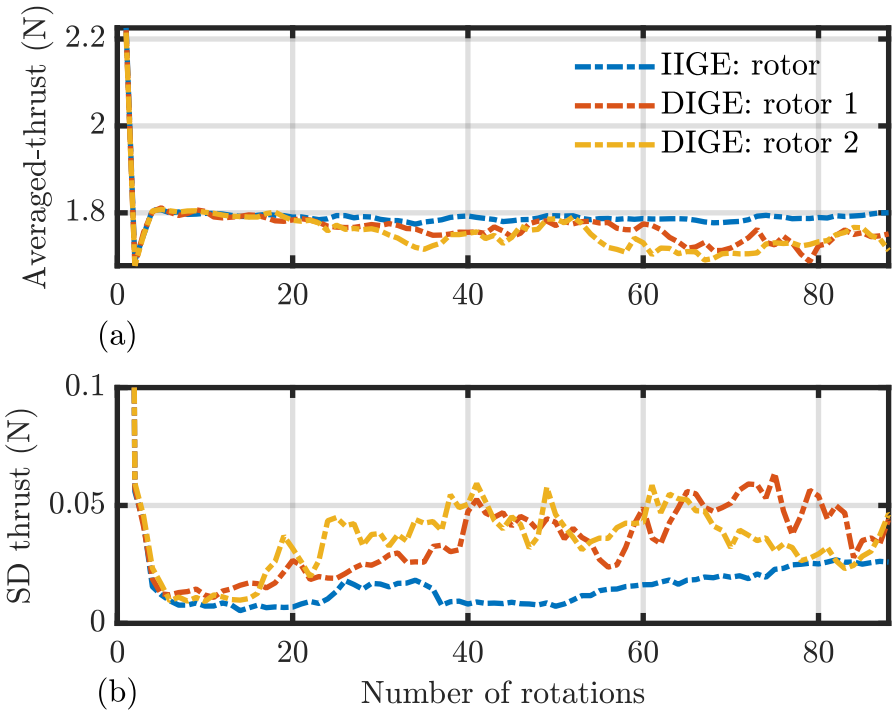

Fig. 4 (a) The time averaged-thrust for the each rotation of the rotor from the DIGE and IIGE, (b) standard deviation of the average thrust for each rotation. These results are from the very coarse grid simulations for $y^+ = 20$.

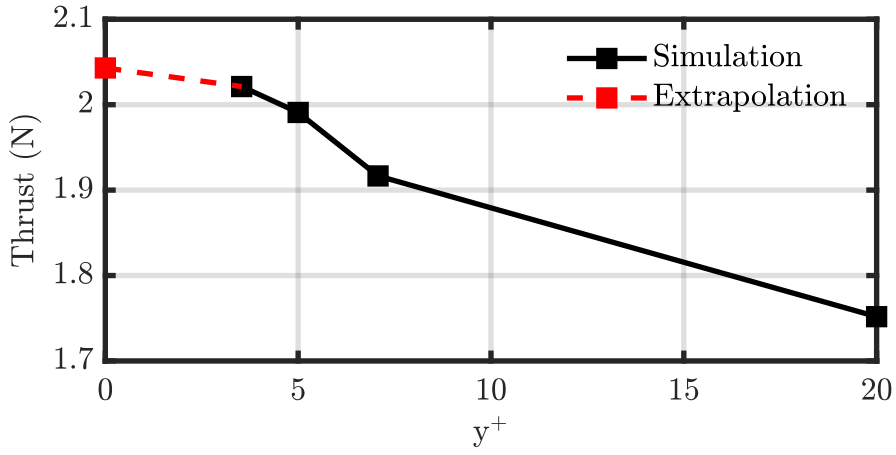

Fig. 5 Trend of the time-averaged mean thrust of two rotors from DIGE for different grid resolution settings.

trend is observed, particularly for the results from $y^+ = 5$ and 3.5, which show nearly identical results. The SPL value for the very coarse case with $y^+ = 20$ demonstrates good agreement below the frequency of 1000 Hz. However, the limited capability of the coarser grid resolution to resolve the turbulence structures re-ingested from the upward fountain flow results in lower values of SPL in a range of frequency between 1500 Hz to 5000 Hz.

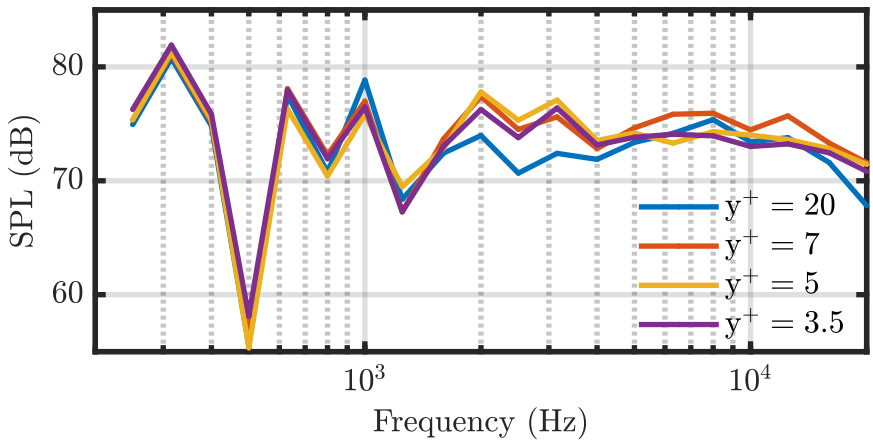

Fig. 6 Comparison of the SPL spectra in one-third octave bands generated from different grid resolutions from DIGE at an observer distance 3R from origin O at polar angle $\theta = 45°$ for azimuthal angle $\phi = 0°$. The SPL values are calculated using the solid FW-H method

B. Flow Field and Aerodynamic Visualization

The instantaneous flow field is visualized using the iso-surface of the constant lambda-2 criterion, see Fig. 7. The color contours represent the non-dimensional axial velocity W/W_{ind}, where $W_{ind} = 14.25$ m/s is the experimental measured induced axial velocity of a single rotor OGE [32]. The tip vortex is clearly visualized close to the blade tip region, exhibiting the formation of helical structures. Due to the presence of the ground plane, the wake decelerates close to the ground plane and expands radially along the wall, resulting in a radially spread wall jet. The wall jet from two rotors impinges at their mirror plane and redirects upward, forming a fountain-like flow. This fountain-like flow mainly tilts towards the right side rotor. Furthermore, the coherent structures travel upwards together with the fountain flow and are re-ingested into the rotors from both sides upon reaching above the rotor disk. These ingested structures undergo distortion near the rotor rotational planes and subsequently interact with the rotor blades, resulting in additional unsteady loading on the blades. This interaction likely contributes to amplifying both tonal and broadband noise levels.

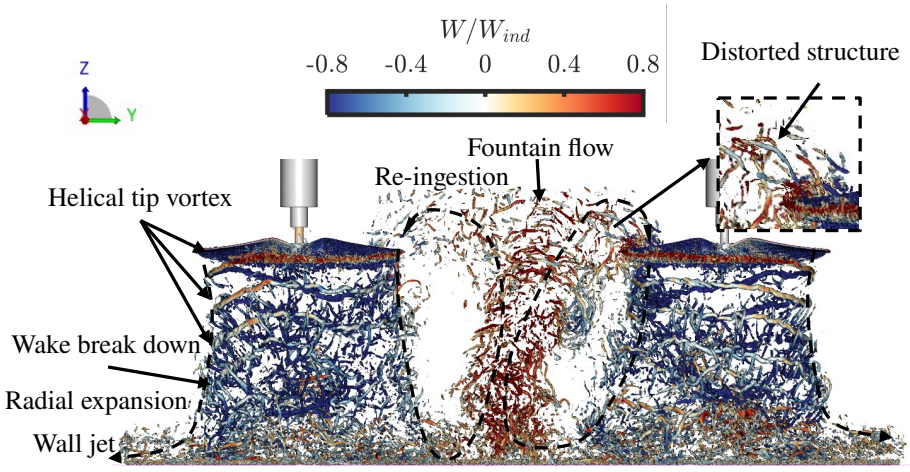

Fig. 7 Front view of the instantaneous turbulence structure visualization using iso-surface constant lambda-2 criterion ($\lambda_2 = -8 \times 10^6$), the color contoured with the non-dimensional axial velocity magnitude W/W_{ind}.

Consistent with findings in prior experimental studies, the re-ingestion observed in the picture above alternates from the left rotor to the right rotor, leading to a cyclic motion of the fountain flow between them. The flow field visualizations used to capture the motion are illustrated in Fig. 8 where the non-dimensional velocity magnitude V_{mag}/W_{ind} is shown. Results from the simulation with grid resolution $y^+ = 7$ are reported. The flow information was captured every 10

degrees of rotor rotation, equivalent to a frequency of 6680 Hz. The sequence begins at t0, with the fountain flow initially leaning towards the left rotor, and flow re-ingestion is clearly observed. Following this stage, at t0 + 51 ms, the fountain flow aligns with the mirror plane of the two rotors and rises above the rotor discs. It then tilts towards the right rotor at t0 + 66 ms, and re-orientates back towards the left rotor at t0 + 126 ms, completing a full cycle movement. Finally, the fountain switches back to the mid-position of the two rotors at t0 + 178 ms. The frequency of this cyclic movement is approximately 7.93 Hz, and a similar phenomenon is observed in the very coarse grid simulation for the y^+ value of 20. These results also demonstrate reasonable agreement with previous experimental findings that reported a frequency of around 8.8 Hz by Dekker *et al.* [9].

Additionally, to visualize the shape and development of the fountain flow, Fig. 9 displays the flow field for the V_{mag}/W_{ind} at the same time instance as presented in Fig. 8, in the z-direction at a height of H = 2.1R. It can be observed that the fountain acts like a barrier, expanding along the mirror plane and spanning approximately from -5R to 5R in the x-direction. Additionally, the effect of the grid resolution on this span range is minimal. Furthermore, due to the re-ingestion effect, the fountain is axisymmetric. Combining the observations from sub-figures (a), (c), and (e) in Fig. 8 and Fig. 9, it appears that the orientation of the fountain flow is not limited to a single direction observed in the co-axis plane. For example, the flow located in the positive x-direction tilts towards the left rotor, while the flow in the negative x-direction leans towards the right rotor. This explains why, even with the fountain flow's direction leaning towards the right rotor, the flow re-ingestion in the left rotor still exists in Fig. 7.

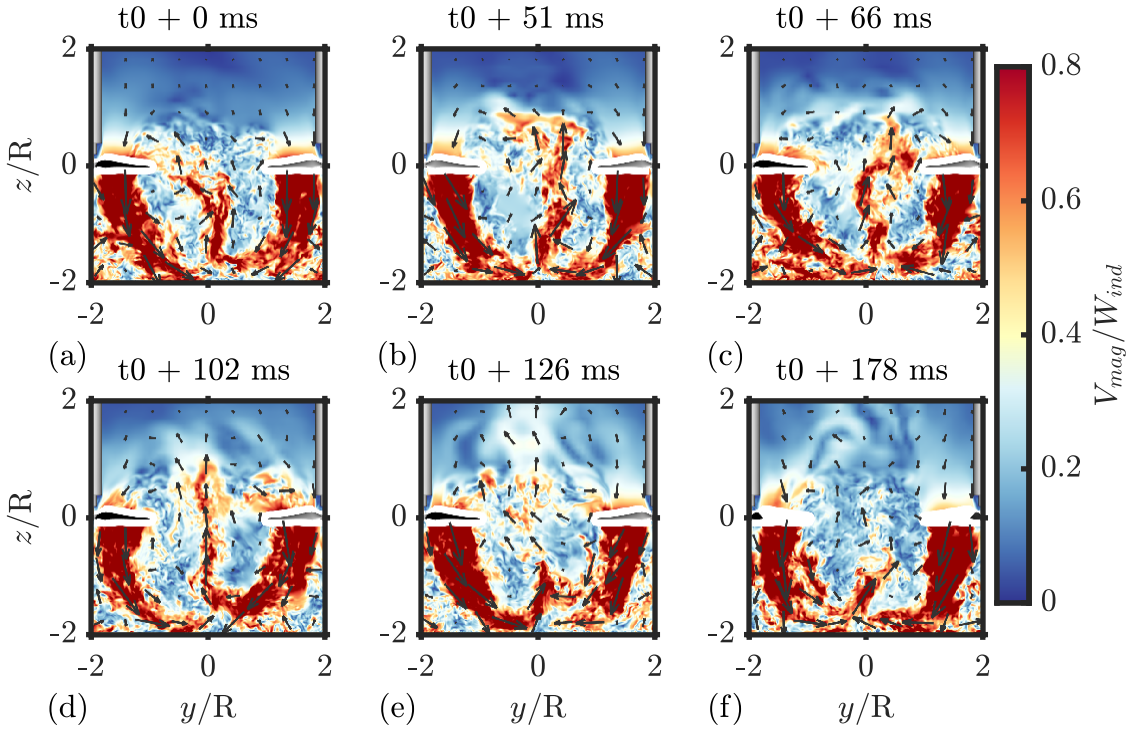

Fig. 8 Front view of the instantaneous normalized velocity magnitude contours V_{mag}/W_{ind} and 2D velocity vectors, within a single cycle of the fountain cyclic movement at the co-axis plane of two rotors.

To investigate the impact of flow re-ingestion on the rotor, an analysis is conducted on surface pressure fluctuations on the propeller for both dual and isolated rotor configurations. This is quantified by using the standard deviation of the propeller surface pressure coefficient with respect to the phase-locked average, denoted as SD C_p. The pressure coefficient C_p is defined as follow:

$$C_p = \frac{p - p_\infty}{0.5\rho_0 V_\infty^2} \tag{2}$$

where p is the static pressure, p_∞ is the free stream static pressure, ρ_0 is the air density and V_∞ is the free stream velocity to the blade. Fig. 10 compares SD C_p for the two configurations with its azimuthal angle locked at $\phi = 90°$.

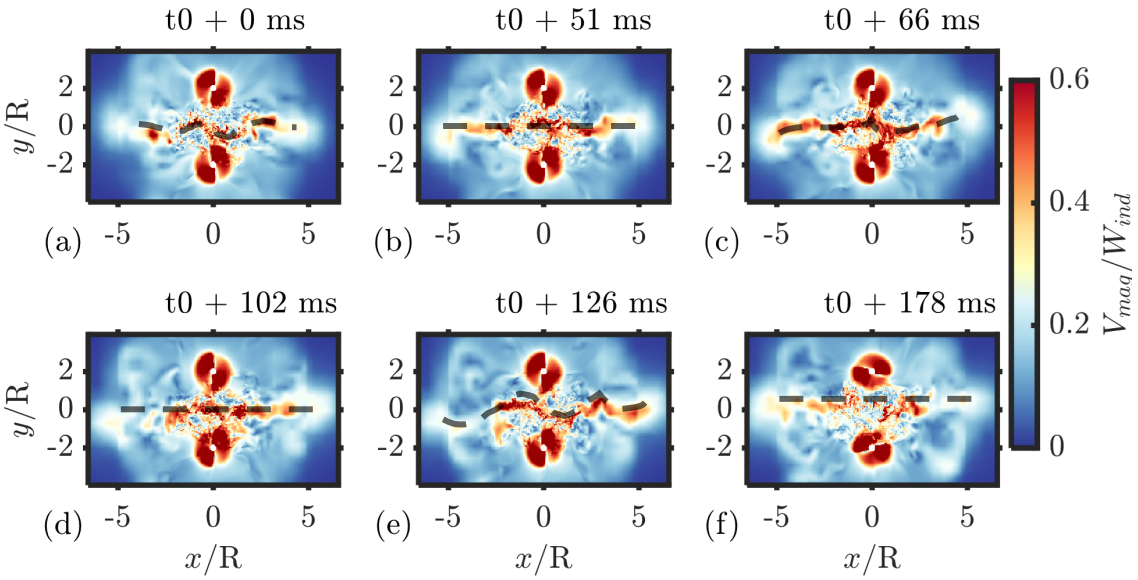

Fig. 9 Top view of the instantaneous normalized velocity magnitude contours V_{mag}/W_{ind} within a single cycle of the fountain cyclic movement at in z-direction height H = 2.1R.

Sub-figures (a, b) and (c, d) depict the suction and pressure sides of the propeller in DIGE and IIGE setups, respectively. The propeller's chordwise and spanwise directions are normalized by the blade radius R, denoted as x_b/R and y_b/R. The positive y_b/R is pointing inwards towards the origin O. In the IIGE, as shown in sub-figure (b, d), both blades exhibit identical SD C_p distributions for both suction and pressure sides. The results indicate significant pressure fluctuations along the spanwise direction of the suction side of the propeller blades. These fluctuations range from 0.3R to 0.9R, with the distributions gradually shifting from the blade's leading edge towards its trailing edge. The highest fluctuations are observed near the blade's trailing edge, specifically between 0.8R and 0.9R. Furthermore, in the DIGE, as presented in sub-figures (a, c), it is evident that when the propeller blade located at positive y_b/R interacts with re-ingested turbulent structures, it results in significant pressure fluctuations on the leading edge region from the blade's radial position at 0.7R to the blade tip on both the suction and pressure sides. This observation is supported by comparing the results from the other blade orients towards negative y_b/R direction where no re-ingestion occurs, as the distributions of SD C_p values are in few different from those of the blade from the IIGE.

C. Aeroacoustics Results

Fig. 11 presents a contour of the near-field instantaneous non-dimensional dilatation field on the co-axis plane of two rotors. The contour reveals the footprint of the acoustic waves generated by the two propellers and reflecting off the ground plane. Moreover, due to the presence of the ground plane, the acoustic waves predominantly radiate in a semi-spherical spreading pattern. Strong constructive and destructive interferences can be observed as the waves propagate to the far-field. Additionally, turbulent wave structures, such as the trajectory of blade tip vortices and the formation of the wall jet near the ground, as well as the fountain flow, are clearly visible. The turbulent structures ingested by the rotor could lead to substantial pressure fluctuations at the blade tip region as discussed previously, thereby enhancing the unsteady loading noise level at higher BPF tones.

Fig. 12 presents the comparison in the near-field SPL spectra obtained directly from a fluid probe and those calculated using both solid and permeable FW-H approaches for the simulation with y^+ = 20. The data are processed using Welch's power spectral density estimate with a Hanning window of 50% overlap and an 8.35 Hz bandwidth. The perfect agreement between the solid and permeable FW-H approaches suggests that the contribution from the quadrupole noise source due to the unsteady flow is negligible, which is consistent with the observation in Fig. 11. In the following parts, the acoustic pressure used for analysis is all generated using the solid FW-H method. Additionally, a quick roll-off of the SPL from fluid probes at higher a frequency is observed, likely attributable to the limited spatial resolution at the current measurement location within the simulation domain. Due to the influence of the wall jet at the

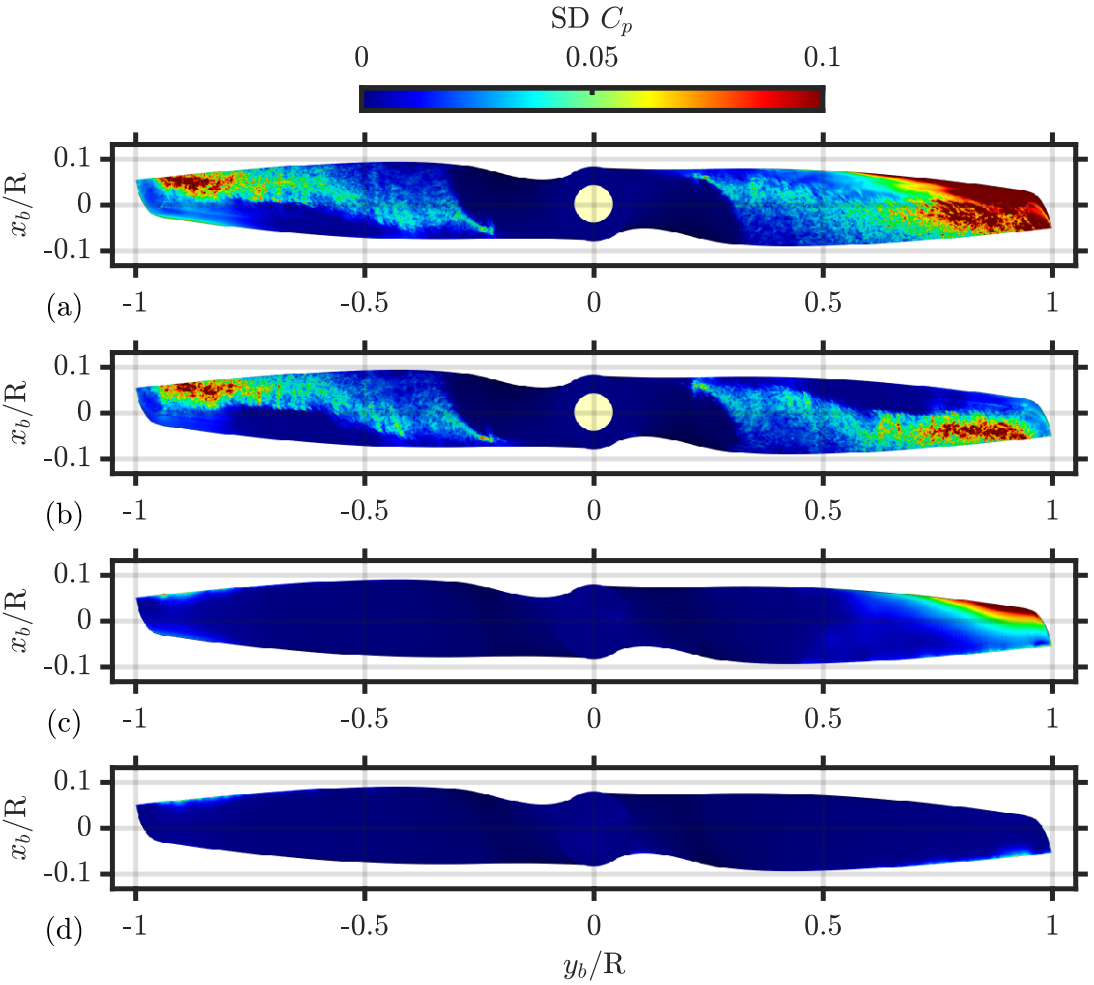

Fig. 10 Comparison of the phase-locked average SD C_p across different configurations with its azimuthal angle locked at $\phi = 90°$, sub-figures (a, b) and (c, d) depict the suction and pressure sides of the propeller for DIGE and IIGE, respectively.

position close to the ground plane, sub-figures (c, d) reveal higher broadband noise in the results obtained from the probe compared to the ones calculated using the FW-H approach. Furthermore, upon comparing the results predicted using the FW-H analogy for both solid and permeable surfaces, a higher level of broadband noise is observed for the microphones located away from the ground plane in contrast to the microphones close to the ground plane. This observation is evident when examining the results presented in sub-figures (a, b) and (c, d).

To assess the impact of flow re-ingestion on the rotor's acoustic performance, a time-frequency analysis of the near-field acoustic pressure from the very coarse grid simulation is conducted. The signals are processed using a Hanning window with a 41.75 Hz bandwidth and 75% overlap. Fig. 13 compares the acoustic results for a fluid point at $\theta = 45°$, where sub-figures (a, c) illustrate the results of total acoustic pressure from DIGE and IIGE and sub-figures (b, d) represent the results from the single rotor only from DIGE and IIGE respectively. The first and the second BPF tones primarily represent the steady loading noise component generated by the propeller, whereas the higher BPF harmonic tones correspond to the unsteady loading noise component. In the results for DIGE, as shown in sub-figures (a, b), the values of the first BPF tone exhibit a decreasing trend, which can be attributed to the drop in average thrust caused by the flow re-ingestion effect, as illustrated in Fig. 4. Additionally, the values for the second and higher BPF tones increase significantly after the 18^{th} rotation, coinciding with fountain flow re-ingestion. This phenomenon is depicted clearly in sub-figure (b), particularly for the second BPF tone, where an intermittent pattern of SPL increments over time is observed, likely a result of the rotor's periodic re-ingestion of the fountain flow, leading to unsteady loading on

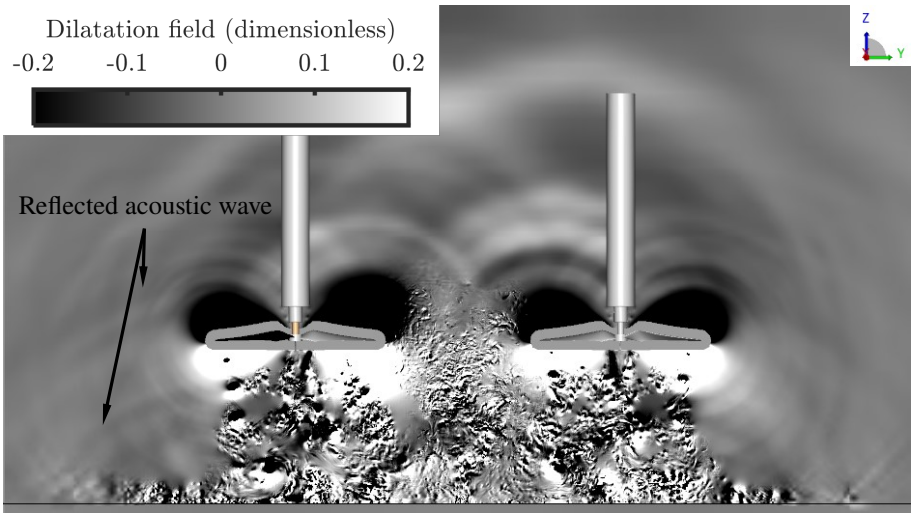

Fig. 11 Contour of the near-field instantaneous nondimensional dilatation field on the co-axis plane of two rotors, results obtained for the simulation with $y^+ = 3.5$.

the rotor blades. Conversely, sub-figure (c, d) shows no significant variation in the SPL values of the BPF tones from the rotor in the IIGE configuration.

In addition to the time-frequency analysis, Fig. 14 compares the corresponding SPL spectra observed at the fluid probes located at $\theta = 45°$ and $\theta = 90°$ between DIGE and IIGE. The acoustic signals are divided into two periods: pre-re-ingestion, covering the signal from the 4th to the 16th rotation, and post-re-ingestion, encompassing the signal from the 20th to the 85th rotation. Sub-figures (a, c) illustrate the total acoustic spectra for DIGE, revealing a notable elevation in SPL values across both broadband and tonal noise components. This increase is observed within the frequency range spanning from the second to approximately the 10th BPF for both $\theta = 45°$ and $\theta = 90°$. This increase is primarily due to the growing unsteady loading on the rotor blades as they interact with the re-ingested turbulent structures, thereby enriching the leading edge noise. This is further illustrated in sub-figures (b, d) by comparing the signals from the single rotor only between the two configurations at pre- and post-re-ingestion status. Firstly, the rotor noise levels generated from IIGE show negligible differences across the spectra between the two periods for both observer locations, as no re-ingestion occurred during the simulation. Furthermore, the pre-re-ingestion noise levels for the rotor from DIGE closely match those generated from IIGE at both observer points. When the re-ingestion occurs, similar to the total noise level, both BPF tones and broadband noise level demonstrate a significant enrichment ranging from the lower frequencies around 2nd to mid-frequencies around the 8th harmonics for $\theta = 45°$ in sub-figure (a). These increases in noise level become weaker when the observer location aligns with the rotor plane, as depicted in sub-figure (d), with only small increments found at the 3rd to 6th BPF tones. Recalling the results presented in Fig. 10, it's evident that the noise level increments are primarily generated from the propeller blade's leading edge region near the blade tip on both the suction and pressure sides. Moreover, both figures illustrate that broadband noise at higher frequencies remains at a similar level between the two conditions.

Fig. 15 illustrates a comparison of the overall sound pressure level (OSPL) in the far-field between the pre-and post-re-ingestion conditions for the results from DIGE. The predictions are performed at 468 semi-spherically distributed microphones. The offset is defined by subtracting the OSPL from the pre-ingestion condition from that of the post-ingestion condition as $\text{OSPL}_\Delta = \text{OSPL}_{post} - \text{OSPL}_{pre}$. First of all, it is evident that higher OSPL values are observed for the microphones placed closer to the vertical axis of the spherical coordinate system, as expected due to the predominance of loading noise in this direction. Moreover, in sub-figures (a-c), the directivity of the total OSPL exhibits a clover-leaf pattern in the azimuthal direction for the observer polar angles closer to the rotor plane. This pattern reveals relatively lower noise levels observed near the azimuthal angles around $\theta = 45°$, 135°, 225° and 315°. A similar finding was also reported by Schiller *et al.* [3], as the side-by-side counter-rotating rotors with 0 phase difference operating at hover condition. Furthermore, the maximum increments of OSPL_Δ are within 3 dB across all the observer microphones, demonstrating a C-shaped pattern with relatively less increments of noise level observed at around $\phi = 0°$. In sub-figures (d-e), both OSPL_{pre} and OSPL_{post} of rotor 1 demonstrate a relatively uniform directivity

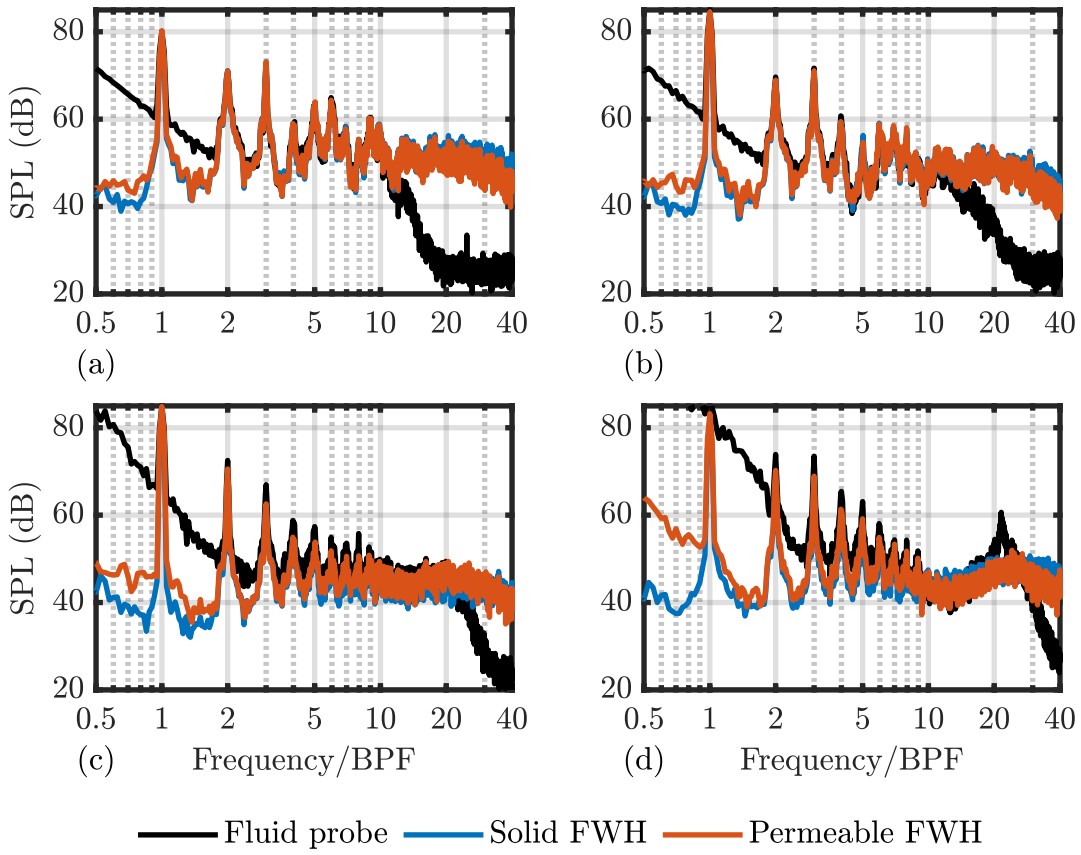

Fig. 12 Comparisons of near-field noise spectra obtained from fluid probe, prediction using FW-H acoustic analogy using solid surface and the permeable surface at a distance of 3R from origin O at different polar angles for (a) $\theta = 30°$**, (b)** $\theta = 60°$**, (c)** $\theta = 90°$ **and (d)** $\theta = 120°$**. Results are from the very coarse grid simulation with** $y^+ = 20$**.**

pattern, however, there is a slight increase in $OSPL_\Delta$ observed at observer locations around azimuthal angles $\phi = 180°$, particularly for polar angles closer to $\theta = 30°$.

To quantify the contribution of both the rotors and the ground plane to OSPL, the results in DIGE from the fine grid simulation with $y^+ = 3.5$ are employed. Fig. 16 presents the results at different polar angles, it is clearly visible that the noise contribution due to the reflection from the ground shows a high directivity pattern in both polar and azimuthal directions. At the polar angle $\theta = 90°$, the contribution from the ground is negligible, whereas it becomes significant for polar angle approaches closer to the vertical axis of the spherical coordinate system. This contribution is represented by an elliptical pattern, with relatively larger contributions observed at azimuthal angles around $\phi = 30°$ and 180°. On average, there is a 2.3 dB increase in OSPL when comparing the total noise level with the combined noise generated from rotor 1 and rotor 2 at $\theta = 90°$.

In Fig. 17, the difference in SPL denoted as SPL_Δ, of the first 10 BPF tones emitted from a single rotor between DIEG and IIGE at various observer locations has been quantified. These results are based on a simulation with $y^+ = 3.5$. The tonal SPL values are evaluated via narrow band integration, considering SPL values within a 1/4 BPF bandwidth and no more than a 20 dB difference from the peak values. It is evident from the results that the most significant enrichment is observed at a polar angle of $\theta = 30°$, with an average SPL_Δ value of 6 dB over the first 10 BPF tones, and a maximum value observed close to 15 dB at the 3^{rd} BPF tone. Conversely, for $\theta = 90°$, the average SPL_Δ value is 1.89 dB, with the maximum value reaching 6 dB at the 5^{th} BPF tone.

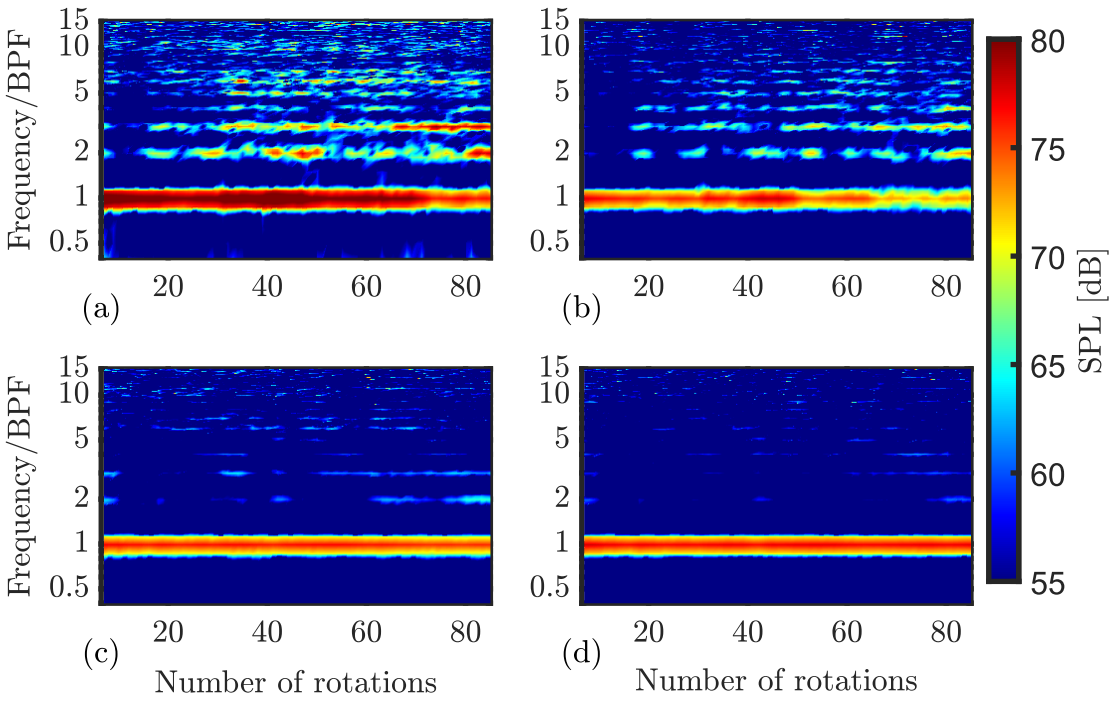

Fig. 13 Time-frequency analysis of the near-field SPL from different configurations for a fluid point at $\theta = 45°$, for the results calculated using solid FW-H approach, where sub-figures (a, c) illustrate the results of total acoustic pressure from DIGE and IIGE and sub-figures (b, d) represent the results from the single rotor only from DIGE and IIGE respectively. Results are from the simulation with $y^+ = 20$.

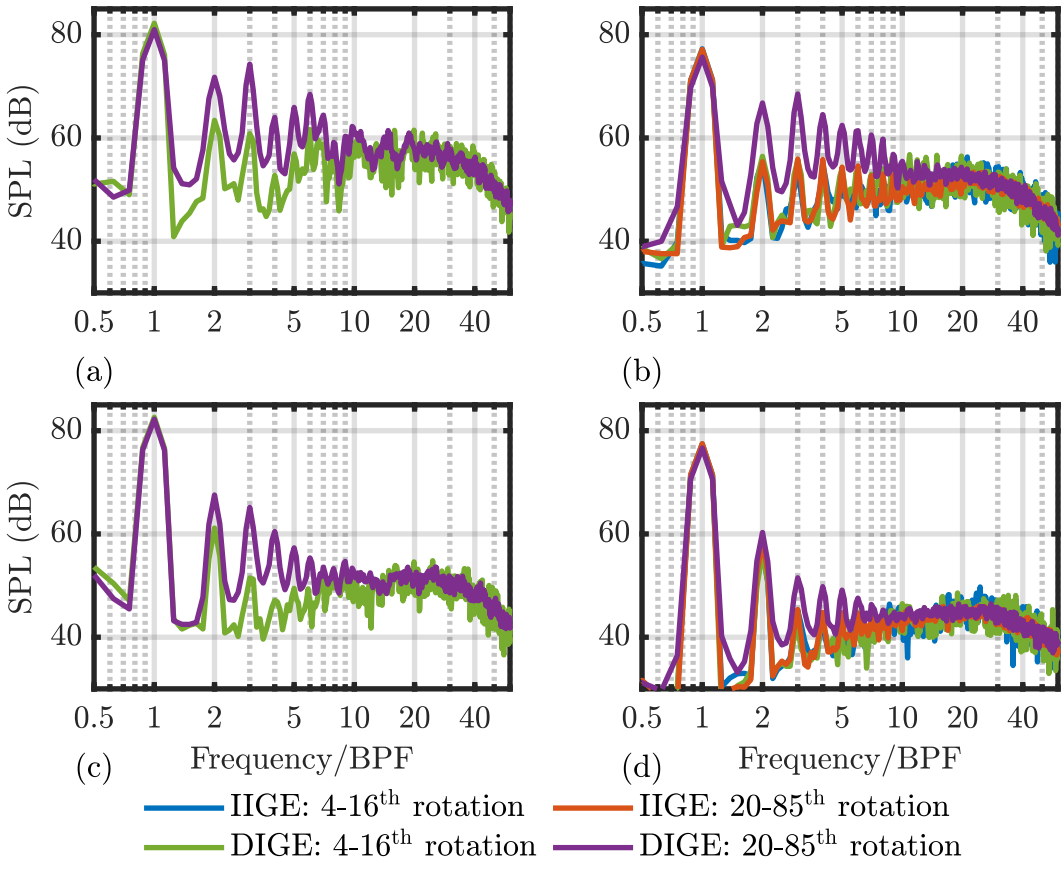

Fig. 14 Comparison of the SPL spectra for the single rotor only between IIGE and DIGE for the fluid probes at (a) $\theta = 45°$, (b) $\theta = 90°$. The signal for both pre-re-ingestion (4^{th} - 16^{th} rotation) and post-re-ingestion (20^{th} - 85^{th} rotation) are illustrated. Results are from the simulation with $y^+ = 20$.

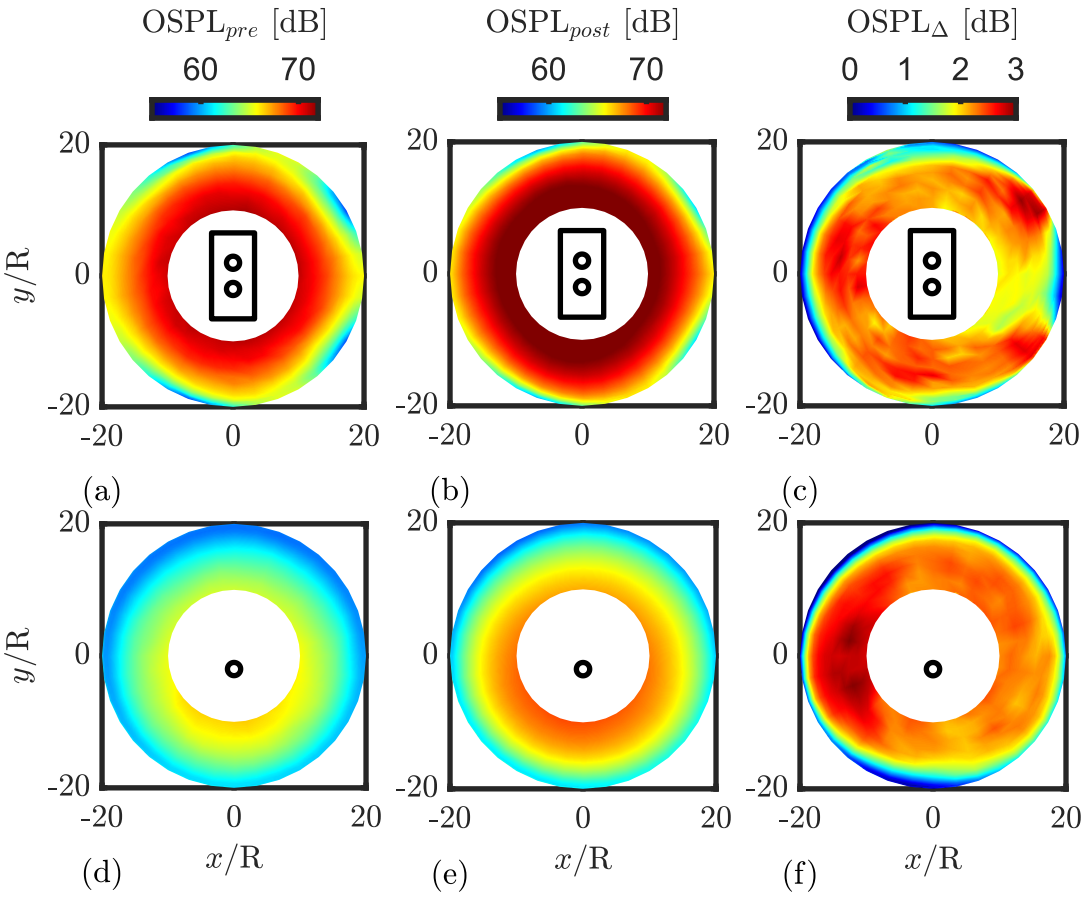

Fig. 15 Comparison of the far-field OSPL between the (a, d) pre-and (b, e) post- re-ingestion condition for the results of DIGE, the top row represents the total noise while the bottom row represents the noise from the rotor 1, the offset OSPL$_{\Delta}$ are presented in sub-figures (c, f) respectively. Results are from the simulation with $y^+ = 20$.

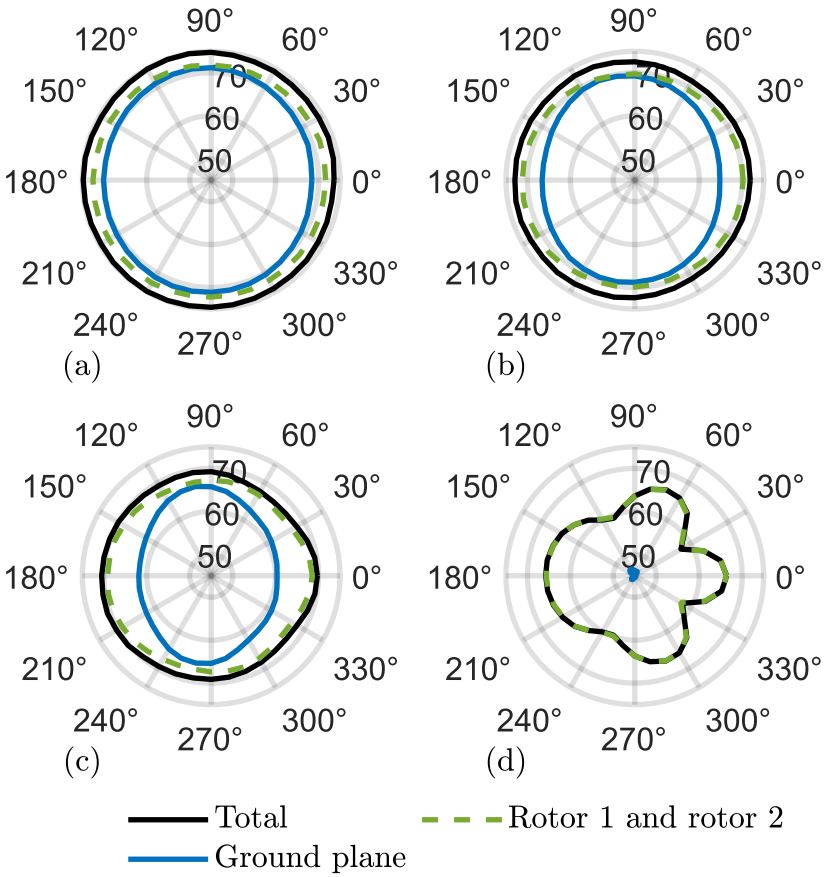

Fig. 16 Contributions to OSPL from the rotors and the ground plane in azimuthal direction at various polar angles, (a) $\theta = 30°$, (b) $\theta = 60°$ and (c) $\theta = 90°$. Results are in DIGE from a fine grid simulation with $y^+ = 3.5$.

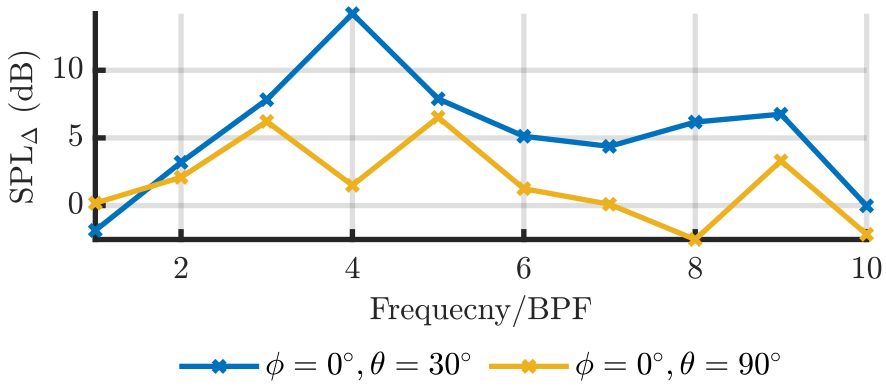

Fig. 17 Plot of the SPL difference, SPL$_\Delta$, of the fist 10 BPF tones emitted from a single rotor between DIEG and IIGE at different observer locations. Results are from the simulation with with $y^+ = 3.5$.

V. Conclusion

A numerical simulation is conducted to study the side-by-side rotor operation IGE at H = 2R and S = 2R conditions. The unsteady interaction between the rotor and the upward fountain flow is observed and shows reasonable agreement with previous experimental results, with the unsteady movement occurring at a frequency two orders of magnitude lower than the rotor BPF. Moreover, the fountain flow primarily develops along the mirror plane of the two rotors, encompassing a span of approximately -5R to 5R. Analysis of the flow field contour above the rotor rotational plane indicates that re-ingestion into both rotors occurs almost simultaneously, contrasting with a unidirectional flow observed on the co-plane of the two rotors. This phenomenon gives rise to a sinusoidal fluctuation and an axisymmetric pattern in the fountain flow.

The simulated rotor thrust from DIGE reveals a 1.4% reduction compared to IIGE results, attributed to the impact of flow re-ingestion. Moreover, the asymptotic value of the average rotor thrust estimated using Richardson extrapolation from DIGE simulation results shows satisfactory agreement with previous findings, with an error of 4.5%. Upon comparing the phase-locked average SD C_p contour on the blades of DIGE and IIGE, it becomes evident that the interaction between the blade and the fountain flow induces additional pressure fluctuations on both the suction and pressure sides of the blade edge region. These pressure fluctuations, resulting in the occurrence of unsteady loading on the blade, likely contribute to the generation of blade leading-edge noise, significantly enhancing blade noise levels across the frequency spectrum from the second BPF to the mid-frequency region for both tonal and broadband noise components. Moreover, this enrichment of the noise level exhibits a stronger directivity pattern in the polar direction, with a maximum of 15 dB enrichment observed at the 3rd BPF tone for observer locations close to the vertical axis away from the rotor plane. The contribution of the acoustic reflection effect from the ground plane to the total noise level exhibits a pronounced directional pattern, aligning closely with findings from the experimental study conducted by Hanson *et al.* [5].

In conclusion, this study reveals the sensitivity of dual-configured small-scale UAV propellers to both aerodynamic and aeroacoustic performance when operating near the ground. Factors such as side-by-side rotor distance, height above the ground plane, and turbulent inflow conditions are found to significantly influence performance. Therefore, these aspects deserve heightened attention during UAV configuration design processes in the future.

Acknowledgments

The authors acknowledge SURF (www.surf.nl) for the support in using the Dutch National Supercomputer Snellius.

References

[1] Tinney, C. E., and Sirohi, J., "Multirotor drone noise at static thrust," *AIAA Journal*, Vol. 56, No. 7, 2018, pp. 2816–2826. https://doi.org/10.2514/1.J056827.

[2] Zhou, T., and Fattah, R., "Tonal noise characteristics of two small-scale propellers," *AIAA paper*, Vol. 4054, 2017, p. 2017. https://doi.org/10.2514/6.2017-4054.

[3] Schiller, N. H., Pascioni, K. A., and Zawodny, N. S., "Tonal noise control using rotor phase synchronization," *Vertical Flight Society Annual Forum and Technology Display (VFS Forum 75)*, 2019.

[4] Bu, H., Wu, H., Bertin, C., Fang, Y., and Zhong, S., "Aerodynamic and acoustic measurements of dual small-scale propellers," *Journal of Sound and Vibration*, Vol. 511, 2021, p. 116330. https://doi.org/10.1016/j.jsv.2021.116330.

[5] Hanson, L., Jawahar, H. K., Vemuri, S. S., and Azarpeyvand, M., "Experimental investigation of propeller noise in ground effect," *Journal of Sound and Vibration*, Vol. 559, 2023, p. 117751. https://doi.org/10.1016/j.jsv.2023.117751.

[6] Smith, B., Healy, R., Gandhi, F., and Lyrintzis, A., "eVTOL Rotor Noise in Ground Effect," *Vertical Flight Society's 77th Annual Forum & Technology Display*, Vol. 1, 2021.

[7] He, X., and Leang, K. K., "Quasi-steady in-ground-effect model for single and multirotor aerial vehicles," *AIAA Journal*, Vol. 58, No. 12, 2020, pp. 5318–5331. https://doi.org/10.2514/1.J059223.

[8] Dekker, H., Ragni, D., Baars, W., Scarano, F., and Tuinstra, M., "Correction: Aerodynamic Interactions of Side-by-Side Rotors in Ground Proximity," *AIAA Journal*, Vol. 61, No. 4, 2023, pp. 1–1. https://doi.org/10.2514/1.J061105.c1.

[9] Dekker, H. N., Baars, W. J., Scarano, F., Tuinstra, M., and Ragni, D., "Unsteady flow behaviour of multi-rotors in ground proximity," *Flow*, Vol. 3, 2023, p. E30. https://doi.org/10.1017/flo.2023.21.

[10] Go, S. T., Kingan, M. J., Bowen, L., and Azarpeyvand, M., "Noise of a shrouded propeller due to ingestion of grid-generated turbulence," *Journal of Sound and Vibration*, Vol. 571, 2024, p. 118044. https://doi.org/10.1016/j.jsv.2023.118044.

[11] Stephenson, J. H., Weitsman, D., and Zawodny, N. S., "Effects of flow recirculation on unmanned aircraft system (UAS) acoustic measurements in closed anechoic chambers," *The Journal of the Acoustical Society of America*, Vol. 145, No. 3, 2019, pp. 1153–1155. https://doi.org/10.1121/1.5092213.

[12] Nardari, C., Casalino, D., Polidoro, F., Coralic, V., Lew, P.-T., and Brodie, J., "Numerical and experimental investigation of flow confinement effects on UAV rotor noise," *25th AIAA/CEAS Aeroacoustics Conference*, 2019, p. 2497. https://doi.org/10.2514/6.2019-2497.

[13] Casalino, D., Romani, G., Pil, L. M., and Colombo, R., "Sensitivity of laminar separation noise from a rotor to inflow turbulence," *AIAA AVIATION 2023 Forum*, 2023, p. 3220. https://doi.org/10.2514/6.2023-3220.

[14] Casalino, D., Romani, G., Zhang, R., and Chen, H., "Lattice-Boltzmann calculations of rotor aeroacoustics in transitional boundary layer regime," *Aerospace Science and Technology*, Vol. 130, 2022, p. 107953. https://doi.org/10.1016/j.ast.2022.107953.

[15] Grande, E., Romani, G., Ragni, D., Avallone, F., and Casalino, D., "Aeroacoustic investigation of a propeller operating at low Reynolds numbers," *AIAA Journal*, Vol. 60, No. 2, 2022, pp. 860–871. https://doi.org/10.2514/1.J060611.

[16] Casalino, D., Grande, E., Romani, G., Ragni, D., and Avallone, F., "Definition of a benchmark for low Reynolds number propeller aeroacoustics," *Aerospace Science and Technology*, Vol. 113, 2021, p. 106707. https://doi.org/10.1016/j.ast.2021.106707.

[17] Brandetti, L., Avallone, F., De Tavernier, D., LeBlanc, B., Ferreira, C. S., and Casalino, D., "Assessment through high-fidelity simulations of a low-fidelity noise prediction tool for a vertical-axis wind turbine," *Journal of Sound and Vibration*, Vol. 547, 2023, p. 117486. https://doi.org/10.1016/j.jsv.2022.117486.

[18] Casalino, D., Hazir, A., and Mann, A., "Turbofan broadband noise prediction using the lattice Boltzmann method," *AIAA Journal*, Vol. 56, No. 2, 2018, pp. 609–628. https://doi.org/10.2514/1.J055674.

[19] Succi, S., *The lattice Boltzmann equation: for fluid dynamics and beyond*, Oxford university press, 2001.

[20] Shan, X., Yuan, X.-F., and Chen, H., "Kinetic theory representation of hydrodynamics: a way beyond the Navier–Stokes equation," *Journal of Fluid Mechanics*, Vol. 550, 2006, pp. 413–441. https://doi.org/10.1017/S0022112005008153.

[21] Chen, S., and Doolen, G. D., "Lattice Boltzmann method for fluid flows," *Annual review of fluid mechanics*, Vol. 30, No. 1, 1998, pp. 329–364. https://doi.org/10.1146/annurev.fluid.30.1.329.

[22] Chen, H., Chen, S., and Matthaeus, W. H., "Recovery of the Navier-Stokes equations using a lattice-gas Boltzmann method," *Physical review A*, Vol. 45, No. 8, 1992, p. R5339. https://doi.org/10.1103/PhysRevA.45.R5339.

[23] Teixeira, C. M., "Incorporating turbulence models into the lattice-Boltzmann method," *International Journal of Modern Physics C*, Vol. 9, No. 08, 1998, pp. 1159–1175. https://doi.org/10.1142/S0129183198001060.

[24] Yakhot, V., and Orszag, S. A., "Renormalization group analysis of turbulence. I. Basic theory," *Journal of scientific computing*, Vol. 1, No. 1, 1986, pp. 3–51. https://doi.org/10.1007/BF01061452.

[25] Wilcox, D. C., et al., *Turbulence modeling for CFD*, Vol. 2, DCW industries La Canada, CA, 1998.

[26] Launder, B. E., and Spalding, D. B., "The numerical computation of turbulent flows," *Numerical prediction of flow, heat transfer, turbulence and combustion*, Elsevier, 1983, pp. 96–116. https://doi.org/10.1016/B978-0-08-030937-8.50016-7.

[27] Williams, J. F., and Hawkings, D. L., "Sound generation by turbulence and surfaces in arbitrary motion," *Philosophical Transactions for the Royal Society of London. Series A, Mathematical and Physical Sciences*, 1969, pp. 321–342. https://doi.org/10.1098/rsta.1969.0031.

[28] Farassat, F., and Succi, G. P., "A review of propeller discrete frequency noise prediction technology with emphasis on two current methods for time domain calculations," *Journal of Sound and Vibration*, Vol. 71, No. 3, 1980, pp. 399–419. https://doi.org/10.1016/0022-460X(80)90422-8.

[29] Casalino, D., "An advanced time approach for acoustic analogy predictions," *Journal of Sound and Vibration*, Vol. 261, No. 4, 2003, pp. 583–612. https://doi.org/10.1016/S0022-460X(02)00986-0.

[30] Di Francescantonio, P., "A new boundary integral formulation for the prediction of sound radiation," *Journal of Sound and Vibration*, Vol. 202, No. 4, 1997, pp. 491–509. https://doi.org/10.1006/jsvi.1996.0843.

[31] Roache, P. J., *Verification and validation in computational science and engineering*, Vol. 895, Hermosa Albuquerque, NM, 1998.

[32] Dekker, H. N., Ragni, D., Baars, W. J., Scarano, F., and Tuinstra, M., "Aerodynamic interactions of side-by-side rotors in ground proximity," *AIAA Journal*, Vol. 60, No. 7, 2022, pp. 4267–4277. https://doi.org/10.2514/1.J061105.